Proceedings of the Korean Nuclear Society Spring Meeting
Gyeongju, Korea, May 2003

Fault Monitoring Techniques for a High Temperature Reduction Reactor

Gee Young Park, Dong Hee Hong, Jae Hoo Jung, Young Hwan Kim, Jae Hyun Jin, and Ji Sup Yoon

Korea Atomic Energy Research Institute
150 Yuseong, Deokjin
Daejeon, Korea 305-353

Abstract

The onset of research into the monitoring techniques for detecting faults in the high temperature reduction reactor commenced in 2001 and a preliminary study was performed in order to support the successful reduction process. The tasks of the fault monitoring techniques are to identify reactor integrity and agitator driving system integrity. Appropriate sensors and related electronic equipment were constructed for the acquisition and analysis of the fault-induced signals. Fault signal acquisitions were performed on the full-scale reduction reactor and the agitator driving experimental facility. Through the fuel oxide reduction experiments in the full-scale reduction reactor, some defects within the reactor were detected and located by use of the acoustic emission signal analysis method. For the agitator driving system, the faults pre-categorized were identified and classified by use of advanced signal analysis and the diagnosis method with measured vibration signals.

1. Introduction

The research for the fault monitoring techniques of the high temperature reduction reactor that is a main process in the advanced spent fuel conditioning process has been performed since 2001 [1]. In the reduction reactor, the fuel oxide reduction takes place by very reactive de-oxidizer (Li) under a high temperature above 600^{o}C. The internal vessel of the reduction reactor is, therefore, to be designed to cope with the thermal stresses from the high temperature distribution and any chemical attack on the internal surface of the reactor. Fig.1 shows the full-scale high temperature reduction reactor whose dimension is 2.4 (H) $\times$ 1.2 (W) $\times$ 1.7 (ID) m. The agitator driving system is installed on the top of the high temperature reduction reactor and stirs the molten salt within the reduction reactor in order to enhance the chemical reaction.

The objective of this study is two fold: one is the development of the monitoring technique for detecting the internal defects such as cracks or corrosions, which will grow to be a high-

risk failure, at the surface of or within the boundary of the internal vessel in the reduction reactor. The other is the monitoring technique for detecting an abnormal status in the agitator driving system in order to increase operational performance and, otherwise, the abnormal rotations may also interfere severely with the monitoring technique for the reduction reactor integrity. From these monitoring results, the operator can recognize the integrities of the internal vessel and the agitator driving system and might set up a schedule for maintenance or decide whether the process should be halted or not.

In order to conduct the monitoring technique for reduction reactor integrity, the acoustic emission (AE) method was employed. For the development of the monitoring technique of the agitator driving system, the vibration signals were measured and analyzed through the advanced signal processing method.

2. Configuration of Data Acquisition System

For acquiring the signals from the internal parts of the high temperature reduction reactor and also from the agitator driving system, the data acquisition system was constructed and its configuration is depicted in Fig.2. As can be seen in Fig.2, two types of the digital signal processing (DSP) boards are installed: one is for AE signal processing and the other for the vibration signal processing. The signal-conditioning module, preceding the DSP board for the vibration signal, pre-processes the vibration signals to have the frequency content of the prescribed bandwidth. The AE signals are pre-processed in the external pre-amplifiers, located near the sensor mounting position, where the AE signals are amplified and filtered out. The pre-amplifier has the amplification gains of 20, 40, and 60dB and the band-pass filter with the range of 100kHz~1MHz. The AE DSP board has very high sampling rates of about 1.2~10MHz and the DSP board for vibration signals has the sampling rates in the range of 12.8~153.6kHz. All of the components described above except the AE pre-amplifiers, the main processor, and peripherals including the stable power supply are enclosed in the portable case shielded carefully against the electronic interferences. Hence, the data acquisition system is very compact and provides a convenient way to acquire data from experiments. The data acquisition system constructed in this way is depicted in Fig.3.

3. Fault Monitoring of Internal Reduction Reactor

The overall configuration of the high temperature full-scale reduction reactor is shown in Fig.4. There are two vessels in the reduction reactor: one is the internal reduction reactor where the fuel oxide powder is deoxidized by inserting the de-oxidizer (Li) into it under the agitation of the molten salt and the other is the protective vessel that maintains the internal materials when any accident occurs. The furnace fully surrounds the vessel and the internal reactor. As can be seen in Fig.4, there is no room for installing AE sensors onto the internal reduction reactor except for the upper flange with the purpose of tightening the internal reactor. In the last year, a preliminary study for the detectablity and characteristics of defect-induced AE signals has been performed on a small-scale reduction reactor [2]. Based on the previous results, more than 3 AE sensors were installed on the full-scale reduction reactor as can be seen in Fig.5 by use of specially manufactured waveguides whose length are 200mm,

much shorter than the waveguide used last year.

In order to perform the location evaluation of AE sources, pre-tests were performed before the operation of the reduction reactor. The arrival time between two consecutive sensor-mounting positions was obtained from the Auto Sensor Test function in AE software. The wave velocities were then calculated by dividing the distance between the two sensors by the arrival time and the proper value for the wave velocity was selected from the linear location calculation with the pencil lead break test. The wave velocity was given as 3300 m/s.

The experiments on the full-scale reduction reactor were performed three times. The first experiment was for the sealing test and the reduction operation was not performed in this experiment. AE sensor installation and data acquisition were engaged in the 2nd and 3rd experiments where the reduction process for 10 kg of oxidized fuel was performed. Full reduction process was operated during 48 hours. In the reduction operations, the salt power was inserted into the internal reduction reactor and then, the furnace began to operate from an ambient temperature to the operating temperature of 650^{o}C. When the salt powder melted down, the agitator driving system was actuated for 10 hours. After 10 hours agitation, the fuel oxide powder was inserted into the internal reduction reactor and the agitation continued for a further 2 hours. After that time, the reduction reaction was carried out by inserting Li powder into the internal reactor for 12 hours and then the valve was opened under agitation. Finally, the power for the furnace was shut off and the experiment was completed.

In the 2nd experiment, many spurious AE signals were detected when the agitator driving system was actuated. Later inspection concluded that the operation signals of agitation had propagated into the AE sensors via contact points between the tightening module of the upper cover on which the agitator driving system was installed and the flange surface of the internal reduction reactor.

Before the 3rd experiment, this misaligned configuration was repaired and it was confirmed, with the sole operation of the agitator driving system, that the agitator operation induced no AE signal. For location calculation, there is no software tool to provide location information for such a complicated configuration as this reduction reactor. And so, a location identification program was constructed to have the pathway compensation for an AE signal propagating from the source position generated at the internal reactor wall to the AE sensors mounted on the waveguides.

In the 3rd experiment, AE signal acquisition was performed for the entire reduction operation processes. In the early stage of heating up the furnace, many AE signals were detected as can be seen in Fig.6 where accumulated AE counts are displayed for 4 AE sensors. Fig.7 depicts the corresponding AE source locations and indicates AE sources are distributed on the entire internal reactor dimension. AE signals were detected rarely as time elapsed, and this implied the reduction reactor was reaching a fully thermal expansion state. After that time, the reduction reactor was silent until the insertion of the oxidized uranium powder into it. When the oxidized powder insertion was completed, AE signals were detected during the agitation of the molten salt and the oxidized uranium power. This is supposed to be due to the collisions of the uranium powder against the internal reactor wall. The location calculation indicated that almost all of the AE sources resided in the range from the surface of the molten salt and the depth of about 400 mm from the flange. When Li was inserted, AE signals generated at locations below 400 mm were detected and the locations of these AE sources are shown in Fig.8. After all operations were finished, the reduction reactor was dismantled and

the wall surface of the internal reduction reactor was inspected visually. This inspection concluded that internal area of the reactor was normal and clean except for the area from the depth of 450 mm to the bottom end of cylindrical shape of the internal reduction reactor. Here, the defects due to corrosion were identified and each AE source location indicated a pit that was produced by spalling down of the corrosion product layer from the wall surface [3]. Fig.9 shows the results of the visual inspection of the internal reduction reactor.

4. Fault Monitoring of Agitator Driving System

The agitator driving system is composed of the magnetic driver and the agitator. In Fig.1, two magnetic drivers are shown on the top of the full-scale reduction reactor. At the temperature of 650^{o}C, the reaction-supporting salt begins to melt down and, at that time, the agitator driving system is actuated for efficient chemical reactions. While the agitator driving system is equipped on the top of the reduction reactor, about half of the rotating axis and the agitator are immersed in the high-temperature molten salt as can be seen in Fig.4. The magnetic driver is rotated by the motor, installed on the side of the reduction reactor, whose rotating axis is arranged in a parallel direction to that of the magnetic driver. Both axes are inter-connected by flexible joint cable that bends in the upper half circle.

The power transmission via the flexible joint cable produces large vibrations of the structure. And, for a series of operations, this induces the looseness of the surrounding bolts. During the high temperature reduction process, fume is generated when the de-oxidizer (Li) powder is inserted into the reactor. After the shut down of the reactor, the decrease in the temperature to the ambient temperature results in the accumulation of fumes in the clearance between the rotating axis and the outer ring, and this makes the agitator driving system rotate intermittently with sudden impact-like vibrations in the next operation. Moreover, the bearing in the outer case of the magnetic driver is sometimes exposed to the fumes emanating from the sample hole during sampling of the salt, which results in the corrosion and wear of the bearings in the magnetic driver near the sample hole. The fault types with possible occurrence in the agitator driving system are categorized in Table 1.

The faults described above increase significantly the burden of regulating the rotating speed of the agitator to the pre-set point, 200 rpm, for the optimal chemical reaction and interfere severely with the other fault monitoring with the acoustic emission method. In order to recognize the fault occurrence and the cause of that fault, the experimental facility of the agitator driving system was constructed and the fault monitoring technique for the agitator driving system was developed. Fig.10 shows the experimental facility of the agitator driving system.

The magnetic driver has the magnetic pulley in the outer case and the magnetic rotor in the center of the magnetic driver. The magnetic pulley rotates by the flexible joint cable and this rotation induces the activation of the magnetic rotor by use of the magnetic force that produces the maximum torque of 6kgf·cm to the agitator attached at the end of the magnetic rotor. The magnetic driver is installed on the top of the mock-up reduction reactor and has a supporting plate that tightens the joint part between the flexible cable end and the magnetic pulley. The supporting plate is connected to the outer shroud of the magnetic driver by two upper and lower bolts. Fig.11(a) and Fig.11(b) show the magnetic driver manufactured and

each component after dismantling the magnetic driver.

In the experiments, two accelerometers are installed on the agitator driving system. As can be seen in Fig.10, one accelerometer is attached to the top of the outer case of the magnetic driver and the other is installed on the outer shroud enclosing the rotating axis.

Through the experiments, the vibration signals for various speeds from 80 to 800 rpm and for various faults were measured and analyzed. The sampling rate was set to 25.6 kHz for all the cases. In this presentation, among all the experimental data, the data for fault types in Table 1 for the set-point rotation speed of 200 rpm were analyzed.

In the monitoring of the rotating machines, the synchronization between the revolution of the rotating axis and the data acquisition is very important for a delicate analysis and the identification of the incipient defect. For the agitator driving system in the high temperature reduction reactor, it is not possible to establish the synchronization process because the motors and the magnetic drivers constructed in the high temperature reduction process are not provided with any revolution measuring unit. Moreover, the motor has no controller that regulating strictly the rotation speed to the prescribed value of 200 rpm and hence, the rotation speed is actually fluctuated around 200 rpm during the operation.

For the analysis, the wavelet transform (WT) with dyadic scales and compact support, orthonormal wavelets [4][5] is applied to the acquired data. The vibration signals are decomposed into the octave band components by the WT. The wavelet used in this decomposition is the ‘ db-10’ wavelet proposed by Daubechies [4]. In the db-10 wavelet, both low-pass and high-pass filters have 20 filter coefficients respectively. This requires more calculations than other Daubechies wavelets but the sharp attenuation at the cut-off frequency can be achieved. Fig.12 shows the results of the wavelet decomposition of the normal rotating signal (Case 1). The rotating signal is decomposed into 8 levels, which results in 8 scales (or details) and 1 approximation. As can be seen in Fig.12, the highly transient signals with higher frequencies are involved at the lower scale levels and, at the highest scale level (8^{th}), the slow signal variation with a low frequency are displayed.

Based on the results of the wavelet decomposition for the vibration signals, the appropriate and compressed feature was extracted from the results of the wavelet transform. The feature extraction was performed by use of the 2^{nd} order moment calculation that calculates the average power for each detail (or scale) from the wavelet decomposition. Fig.13 shows the feature extraction by the 2^{nd} order moment calculation. As can be seen in Fig.13, the faults can be discriminated from each other when one inspects carefully the simple trends and characteristics of 2^{nd} order moment calculations. As a demonstration of the consistent trend, Fig.14 shows the features of Case 1 for the test data blocks. These features show the distinguishable trend but one of them is a little distorted.

For the implementation of the diagnosis based on the features extracted from the 2^{nd} order moment calculation, the neural network classifier based on the adaptive resonance theory (ART) [6], which is called the fuzzy ARTMAP [7] in neural network literatures, is constructed. The ART has the architecture where a new feature vector is learned without modifying the existing information for different features. Hence, it can preserve the previously learned knowledge while continuing to learn new things.

The fuzzy ARTMAP is a class of neural networks that perform incremental supervised learning of recognition categories and multidimensional maps in response to input vectors presented in an arbitrary order. Fig.15 shows the architecture of the fuzzy ARTMAP where

two fuzzy ART modules (ART_a and ART_b) and a map field F^{ab} are involved. The input vectors **A** of dimension M_a and **B** of dimension M_b are the feature vectors respectively corresponding to the symptom and the cause. The components of each input vector are analog or binary values within the range of [0,1]. Each component of the input vector represents a feature item that is grouped to establish the representative feature.

When input vectors are given, input vector **A** is transferred to the field F_0^a where the complement coding is performed based on the input vector. In the field F_0^a of Fig.15, $\mathbf{A}^c$ means the complement of **A**, that is, $A_i^c = 1 - A_i$ for i = 1,⋯,M_a. By complement coding, the dimension of the input at the fuzzy ART_a increases by $2M_a$. This complement coding is necessary for prohibiting the so-called category proliferation [8]. The $\mathbf{W}_j^a$ is an $1\times 2M_a$ vector such that $\mathbf{W}_j^a = [W_{j,1}^a,\cdots,W_{j,2Ma}^a]$ and the subscript j is *j*th node at the field F_2^a. All initial values of $\mathbf{W}_j^a$ are set to 1. After the complement coding, $\mathbf{I}^a$ is presented to the input terminal of the field F_1^a and this becomes $\mathbf{x}^a$ and is fed up to the field F_2^a through the weight vector $\mathbf{W}_j^a$ for j = 1,⋯,N_a where N_a is the number of nodes in the field F_2^a.

For the input vector $\mathbf{I}^a$ and F_2^a node j, the choice function, T_j, is defined by

$$T_j(\mathbf{I}^a) = |\mathbf{I}^a \wedge \mathbf{W}_j^a| / (\alpha + |\mathbf{W}_j^a|), \text{ for } j = 1,\cdots,N_a, \quad (1)$$

In Eq.(1), α is called the conservative parameter that has a very small value. And, for M dimensional vectors **p** and **q**, $\mathbf{p}\wedge\mathbf{q} = \{\min(p_i, q_i): \text{for } \forall i\}$ and $|\mathbf{p}| = \Sigma_{i=1}^{M}|p_i|$. Among the values of T_j, the winning node indexed by J is selected by $T_J = \max\{T_j: j = 1,\cdots,N_a\}$. The output vector $\mathbf{y}^a$ is obtained by setting all components of $\mathbf{y}^a$ to zero but the *J*th component with 1. Then this output vector $\mathbf{y}^a$ goes down to the field F_1^a where $\mathbf{x}^a$ now becomes $\mathbf{x}^a = \mathbf{I}^a \wedge \mathbf{W}_J^a$. If the following condition is satisfied;

$$|\mathbf{x}^a| = |\mathbf{I}^a \wedge \mathbf{W}_J^a| \geq \rho_a |\mathbf{I}^a|, \quad (2)$$

then, it is said the resonance state occurs and the learning is performed by

$$\mathbf{W}_J^a(\text{new}) = \beta(\mathbf{I}^a \wedge \mathbf{W}_J^a(\text{old})) + (1-\beta)\,\mathbf{W}_J^a(\text{old}). \quad (3)$$

In Eq.(3), β is a constant in the range of [0,1] and ρ_a in Eq.(2) is called the vigilance parameter having a value of [0,1] and set to a low value ρ_a^{base} at the initial stage. If the condition is not satisfied, the reset operation occurs in such a way that the value of y_J is set to zero and *J*th node of F_2^a is prohibited from being the winning node for a further presentation of the input vector $\mathbf{I}^a$, And the input vector $\mathbf{I}^a$ is presented again and calculations described above are iterated until the resonance state of Eq.(2) is reached. The operations of the fuzzy ART_b, when the input vector **B** is given and the number of the output node is set to N_b, are the same as in the fuzzy ART_a. The winning node at F_2^b is denoted by K.

The map field F^{ab} is activated whenever one of the fuzzy ART modules (fuzzy ART_a and ART_b) is in the resonance state. If node J of F_2^a is chosen, then weight $\mathbf{W}_J^{ab}$ ($\mathbf{W}_J^{ab} = [W_{J,1}^{ab},\cdots,W_{J,Nb}^{ab}]$) activates the field F^{ab}. If node K of F_2^b is selected, then the node K in F^{ab} is activated by one-to-one pathways between F_2^b and F^{ab}. If both fuzzy ART_a and ART_b are active, then F^{ab} becomes active only if the fuzzy ART_a predicts the same category as the fuzzy ART_b via the weight vector $\mathbf{W}_J^{ab}$ (that is, $W_{J,K}^{ab} \neq 0$). The output vector $\mathbf{x}^{ab}$ at the map field F^{ab} is calculated by $\mathbf{x}^{ab} = \mathbf{y}^b \wedge \mathbf{W}_j^{ab}$, if both F_2^a and F_2^b are active.

With the values of $\mathbf{x}^{ab}$ for both fields F_2^a and F_2^b active, if the following condition is satisfied;

$$|\mathbf{x}^{ab}| \geq \rho_{ab}|\mathbf{y}^b|, \quad (4)$$

the mapping or prediction procedure is completed. If the condition Eq.(4) is not satisfied, the

vigilance parameter ρ_a in the fuzzy ART_a is increased from ρ_a^{base} by a small value in order for $| \mathbf{I}^a \wedge \mathbf{W}_J^a | < \rho_a | \mathbf{I}^a |$ to occur, which ultimately leads to activation of another F_2^a node J satisfying Eq.(2) and Eq.(4) for the input vector $\mathbf{I}^a$. At initial, all the components in $\mathbf{W}_j^{ab}$ (for $j = 1,\cdots,N_a$) are set to 1. When the fuzzy ARTMAP is under the training phase and F_2^a node J and F_2^b node K are active, $W_{J,K}^{ab} = 1$ and $W_{J,k}^{ab} = 0$ (for $k = 1,\cdots,N_b$ and $k \neq K$).

For classifying the faults in the agitator driving system, six types of data sets are acquired from the experimental facility. For off-line training of the fuzzy ARTMAP, one set for each fault is selected from the data sets and the remainder data sets are used to test the fuzzy ARTMAP diagnosis performance. Table 2 presents the number of the training and test data for each fault type. In the training phase, training data for each fault is presented just once to the fuzzy ARTMAP and single learning iteration is selected.

The parameters in the fuzzy ARTMAP are given by $\beta = 1$, $\alpha = 0.0001$, $\rho_a = 0.8$, $\rho_b = 0.8$, and $\rho_{ab} = 0.8$. The input vector $\mathbf{A}$ for the fuzzy ART_a is the 2^{nd} momentum values for 8 details (or scales) and 1 approximation from the wavelet decomposition and thus, has a dimension of $M_a = 9$. All input vectors for the fuzzy ART_a are normalized into the range of [0,1] by a constant value of 4.7. The input vector B for the fuzzy ART_b contains the binary values with a single 1 that represents a specific fault and has a dimension of $M_b = 6$. The brief descriptions and values of the parameters in the fuzzy ARTMAP are summarized in Table 2.

The learning time for the fuzzy ARTMAP at the training phase is extremely short because of the single learning iteration. After single input presentation, the fuzzy ARTMAP shows the perfect classification for the training data set when the same input vectors are presented at the test mode. For test data sets, the fuzzy ARTMAP also shows the correct fault identification performance though the test data are distorted or a little bit different from the training data.

5. Conclusions

In this presentation, the fault monitoring techniques are presented in order for monitoring and diagnosing the integrity of the internal reduction reactor and the status of the agitator driving system in the high temperature reduction reactor. For monitoring the internal reduction reactor, the AE method was employed to detect the internal wall defects during reduction operation. For the agitator driving system, the vibration signals were measured on the experimental facility where the pre-categorized faults were induced. The advanced signal analysis method and the robust classifier were employed for identifying the fault occurrence and cause. This activity will help improve the safe operation of the advanced spent fuel conditioning process or any other thermal processes.

References

[1] G. Y. Park, et al, “Development of Fault Signal Analysis Technique for Advanced Spent Fuel Management Process”, Technical Report, KAERI/TR-2156, 2002. (in Korean)

[2] G. Y. Park, et al, “Development of Fault Monitoring System for Advanced Spent Fuel Conditioning Process”, PBNC 2002 (The 13th Pacific Basin Nuclear Conference),

Session:TS-9B, no.3, pp.1-8, Oct. 21~25, Shenzhen, China, 2002.
[3] G. Y. Park, et al, "Development of Fault Monitoring System by Acoustic Emission for Thermal Reduction Reactor", J. of KNS, vol.35, no.1, pp.25-34, 2003.
[4] I. Daubechies, *Ten Lectures on Wavelets*, SIAM, Philadelphia, PA, 1992.
[5] C. S. Burrus, R. A. Gopinath, and H. Guo, *Introduction to Wavelets and Wavelet Transforms*, Prentice Hall, 1998.
[6] G. A. Carpenter and S. Grossberg, "The ART of Adaptive Pattern Recognition by a Self-Organizing Neural Network", Computer, pp.77~88, March 1988.
[7] G. A. Carpenter, S. Grossberg, N. Markuzon, J. H. Reynolds, and D. B. Rosen, "Fuzzy ARTMAP: A Neural Networl Architecture for Incremental Supervised Learning of Analog Multi-Dimensional Maps", IEEE Trans. on Neural Networks, vol.3, no.5, pp.698~713, 1992.
[8] G. A. Carpenter, S. Grossberg, and D. B. Rosen, "Fuzzy ART: Fast Stable Learning and Categorization of Analog Patterns by an Adaptive Resonance System", Neural Networks, vol.4, pp.759~771, 1991.

Table 1. Fault Types Categorized

Fault Type	Contents
Case 1	Normal Rotation
Case 2	Looseness of One of Upper Bolts
Case 3	Looseness of Lower Bolts
Case 4	Looseness of Upper Bolts
Case 5	Bearing Defect
Case 6	Clearance Blocking

Table 2. Data Sets and Configuration of Fuzzy ARTMAP

Training Data Sets	♦ Data Set: 6 Sets • Case 1: 1 Set • Case 2: 1 Set • Case 3: 1 Set • Case 4: 1 Set • Case 5: 1 Set • Case 6: 1 Set
Test Data Sets	♦ Data Set: 27 Sets • Case 1: 7 Sets • Case 2: 4 Sets • Case 3: 5 Sets • Case 4: 3 Sets • Case 5: 4 Sets • Case 6: 4 Sets
Training Type & Parameters	• Off-Line Learning, Single Input Presentation, and Single Learning Iteration • Fast Learn: $\beta = 1$ • Conservative Limit Value: $\alpha = 0.0001$ • Vigilance and Matching Criterion: $\rho_a = 0.8$, $\rho_b = 0.8$, and $\rho_{ab} = 0.8$

Fig.1 Full-Scale High Temperature Reduction Reactor

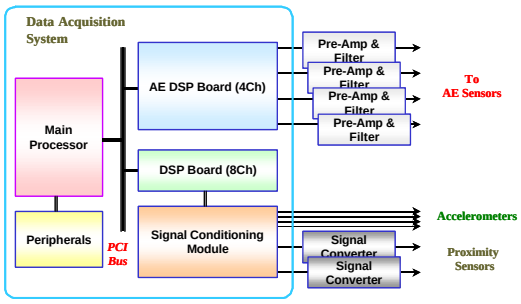

Fig.2 Configuration of Data Acquisition System

Fig.3 Data Acquisition System

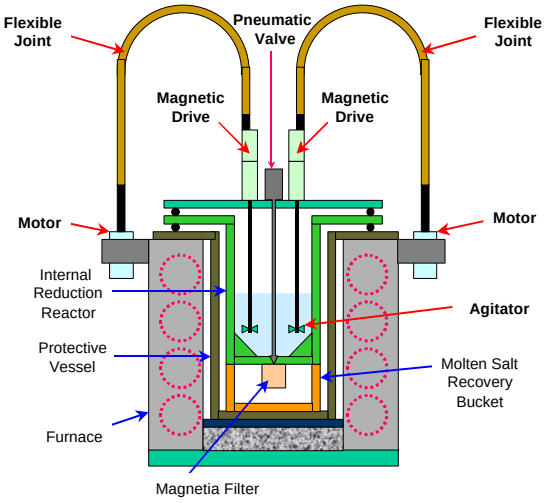

Fig.4 Configuration of Reduction Reactor

Fig.5 AE Sensors and Waveguides Mounted

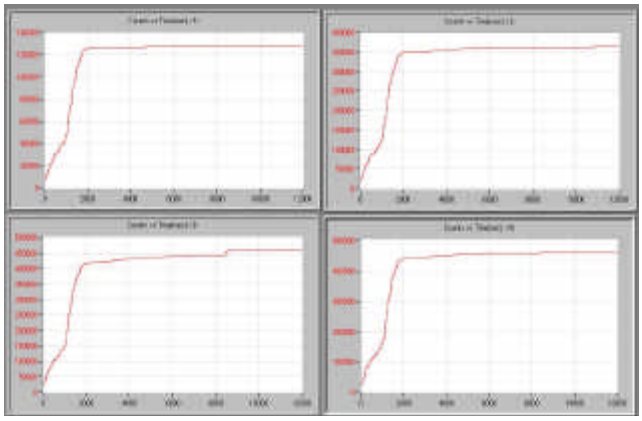

Fig.6 Accumulated AE Counts

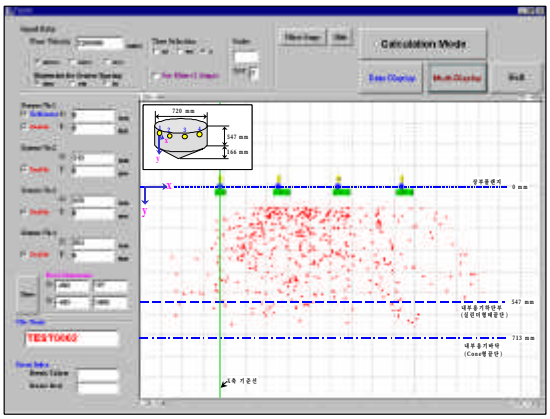

Fig.7 AE Source Location at Initial Heating

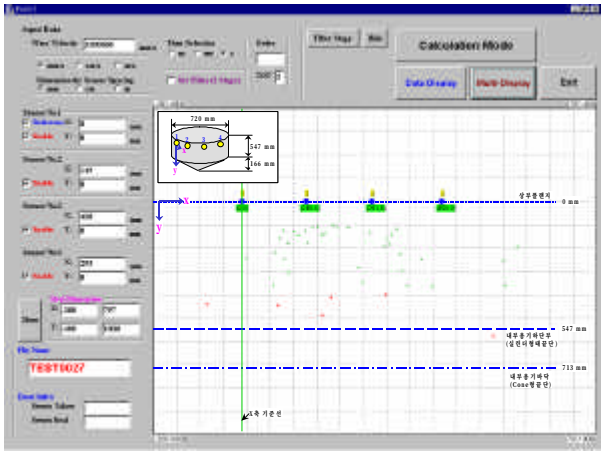

Fig.8 AE Source Locations during Reduction Operation

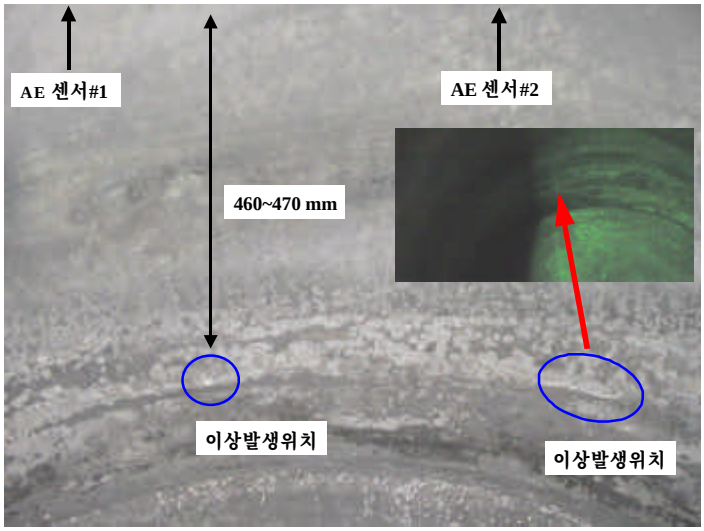

Fig.9 Visual Inspection Result

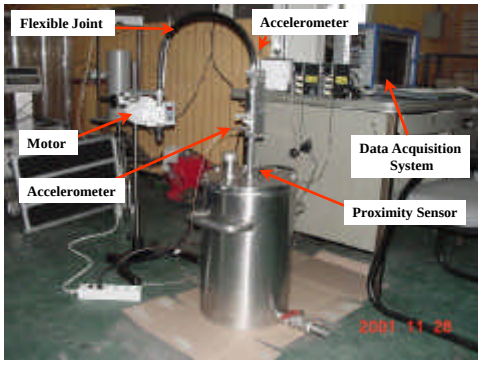

Fig.10 Experimental Facility for Agitator Driving System

Fig.11(a) Magnetic Driver Manufactured

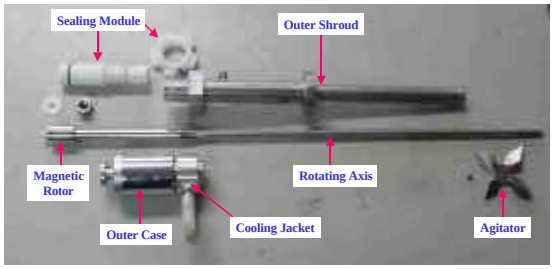

Fig.11(b) Components of Magnetic Driver

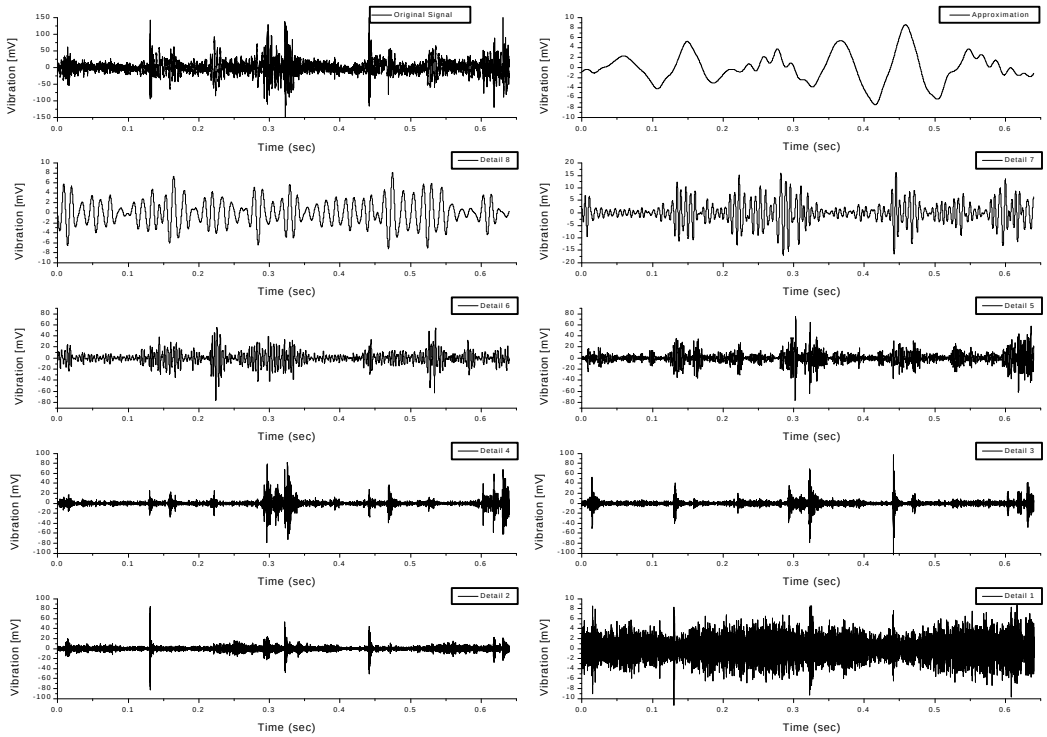

Fig.12 Wavelet Analysis for Case 1

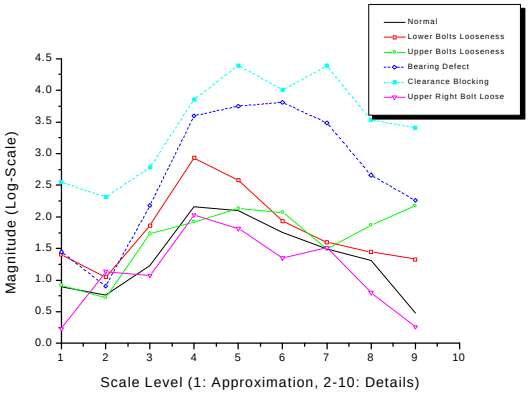

Fig.13 Feature Extraction

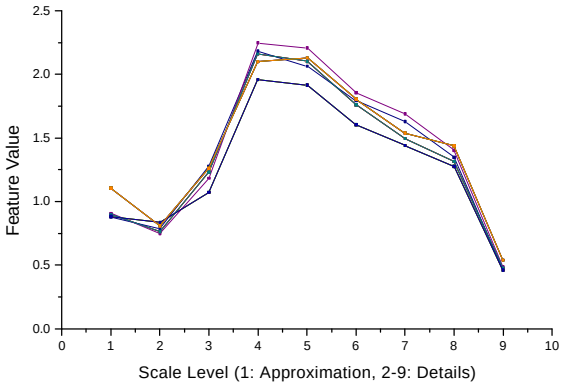

Fig.14 Features for Case 1

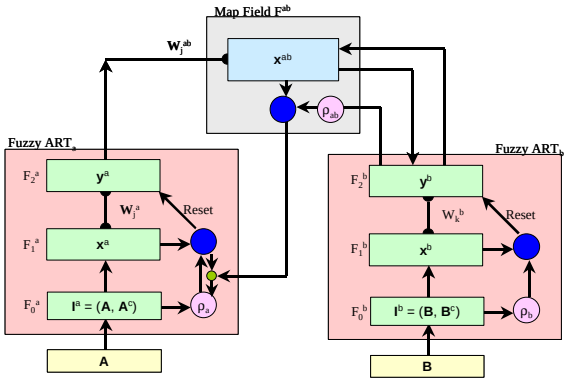

Fig.15 Configuration of Fuzzy ARTMAP